


Glueball spectroscopy in lattice QCD using gradient flow

Keita Sakai^{*} and Shoichi Sasaki[†]*Department of Physics, Tohoku University, Sendai 980-8578, Japan* (Received 28 November 2022; accepted 6 February 2023; published 27 February 2023)

Removing ultraviolet noise from the gauge fields is necessary for glueball spectroscopy in lattice QCD. It is known that the Yang-Mills gradient flow method is an alternative approach instead of link smearing or link fuzzing in various aspects. In this work we study the application of the gradient flow technique to the construction of the extended glueball operators. We examine a simple application of the gradient flow method, which has some problems in glueball mass calculations at large flow time because of its nature of diffusion in space-time. To avoid this problem, the spatial links are evolved by the “spatial gradient flow”, that is defined to restrict the diffusion to spatial directions only. We test the spatial gradient flow in calculations of glueball two-point functions and Wilson loops as a new smearing method, and then discuss its efficiency in comparison with the original gradient flow method and the conventional method. Furthermore, to demonstrate the feasibility of our proposed method, we determine the masses of the three lowest-lying glueball states, corresponding to the 0^{++} , 2^{++} , and 0^{-+} glueballs, in the continuum limit in pure Yang-Mills theory.

DOI: [10.1103/PhysRevD.107.034510](https://doi.org/10.1103/PhysRevD.107.034510)

I. INTRODUCTION

The existence of composite states consisting solely of gluons, called glueballs, is one of the important predictions of QCD. Since none of them have been identified in experiments as a glueball state, the lattice QCD results play an essential role in studying properties of the glueball states including their masses. However, ultraviolet noise from the gauge fields makes it difficult to calculate the glueball spectrum in lattice QCD. Therefore, noise reduction techniques such as the single-link smearing or the double-link fuzzing procedure plays an increasingly important role in the construction of the extended glueball operators.

Various smearing techniques such as APE smearing [1], HYP-smearing [2], and stout smearing [3] are developed for many purposes, while the fuzzing approach is proposed for a specific purpose that requires a significant improvement of having a better overlap with the glueball ground states [4]. In several previous works on the lattice glueball mass calculations [5–8], some sophisticated combinations of both the single-link smearing and the double-link

fuzzing schemes are conventionally adopted (denoted as the conventional approach).

Recently, it was found that the Yang-Mills gradient flow method [9] is an alternative approach instead of the smearing in various aspects (e.g., the computation of topological charge [10]). Indeed, the gradient flow equation can be regarded as a continuous version of the recursive update procedure in the stout-link smearing with the small smearing parameter [9,10]. Therefore, in this study, we investigate the application of the gradient flow technique to the glueball calculation and also demonstrate its effectiveness in comparison to the conventional approach.

This paper is organized as follows. In Sec. II, after a brief introduction of the original Yang-Mills gradient flow, we describe our proposal of “spatial gradient flow” as a new smearing method. In Sec. III, we give a short outline of how to construct glueball two-point functions based on space-like Wilson loops. In Sec. IV, we first briefly summarize the numerical ensembles used in this study. Then we present results of the static quark potential computed with the spatial gradient flow on every ensemble. Section V gives the features of the spatial gradient flow in glueball spectroscopy. The results of glueball masses obtained by the spatial gradient flow are summarized in Sec. VI. Finally, we close with summary in Sec. VII.

II. CALCULATION METHOD I: GRADIENT FLOW METHOD

In this section, we first provide a brief review of the original Yang-Mills gradient flow, which makes the Wilson

^{*}sakai@nucl.phys.tohoku.ac.jp[†]ssasaki@nucl.phys.tohoku.ac.jp

Published by the American Physical Society under the terms of the Creative Commons Attribution 4.0 International license. Further distribution of this work must maintain attribution to the author(s) and the published article's title, journal citation, and DOI. Funded by SCOAP³.

flow diffused in the four-dimensional space-time, in Sec. II A. As reported in Ref. [11], a simple application of the gradient flow technique to the glueball calculation has some problem in measuring the glueball mass from the two-point function. We thus propose the ‘‘spatial gradient flow’’ as a new smearing method, which is described in Sec. II B.

A. Original gradient flow

The Yang-Mills gradient flow on the lattice is a kind of diffusion equation, where the link variables $U_\mu(x)$ evolve smoothly as a function of fictitious time τ (denoted as flow time) [9]. The associated flow $V_\mu(x, \tau)$ of the link variables (hereafter called the Wilson flow) driven by the gradient of the action with respect the link variables [9]. The simplest choice of the action of the link variables $U_\mu(x)$ is the standard Wilson plaquette action,

$$S_W[U] = \frac{2}{g_0^2} \sum_{x, \mu > \nu} \text{Tr} \{ 1 - \text{Re}[U_\mu(x) U_\nu(x + \hat{\mu}) \times U_\mu^\dagger(x + \hat{\nu}, \tau) U_\nu^\dagger(x)] \}, \quad (1)$$

where g_0 is the bare coupling. The flowed link variables $V_\mu(x, \tau)$ are defined by the following equation with the initial conditions $V_\mu(x, 0) = U_\mu(x)$,

$$\frac{\partial}{\partial \tau} V_\mu(x, \tau) \cdot V_\mu^{-1}(x, \tau) = -g_0^2 \partial_{x, \mu} S_W[V], \quad (2)$$

where $S_W[V]$ denotes the standard Wilson plaquette action in terms of the flowed link variables (see Appendix A for the definition of the link derivative operator $\partial_{x, \mu}$ and the explicit expression of $\partial_{x, \mu} S_W$).

According to Eq. (2), the link variables are diffused in the four-dimensional space-time, so that the Wilson flow is approximately spread out in a Gaussian distribution with the diffusion radius (or length) of $R_d = \sqrt{8\tau}$ [9]. Although such smearing procedure works well with the longer flow time, too much smearing will destroy or hide the true temporal correlation of the glueball two-point function due to the overlap of two glueball operators given by the Wilson flow as discussed in Ref. [11]. Therefore, the longer flow is not applicable for the glueball spectroscopy to avoid over smearing, that was observed in Ref. [12].

B. Spatial gradient flow as a new smearing method

As described in Sec. II A, the previous attempt to apply the gradient flow to the glueball spectroscopy is not fully satisfactory [12]. We propose the ‘‘spatial gradient flow’’ as a new smearing method in order to overcome the limited usage of the Wilson flow due to over smearing. The spatial gradient flow is defined to restrict the diffusion to spatial directions only, so that the spatial links $U_i(x)$ are evolved into the spatial Wilson flow $\mathcal{V}_i(x, \tau)$ as the initial

conditions of $\mathcal{V}_i(x, 0) = U_i(x)$ in the following gradient flow equation:

$$\frac{\partial}{\partial \tau} \mathcal{V}_i(x, \tau) \cdot \mathcal{V}_i^{-1}(x, \tau) = -g_0^2 \partial_{x, i} S_{sW}[\mathcal{V}_i(x, \tau)]. \quad (3)$$

Here, S_{sW} denotes the spatial part of the standard Wilson plaquette action,

$$S_{sW}[\mathcal{V}_i(x, \tau)] = \frac{2}{g_0^2} \sum_{x, i > j} \text{Tr} \{ 1 - \text{Re}[\mathcal{V}_i(x, \tau) \mathcal{V}_j(x + \hat{i}, \tau) \times \mathcal{V}_i^\dagger(x + \hat{j}, \tau) \mathcal{V}_j^\dagger(x, \tau)] \}, \quad (4)$$

where the plaquette values are composed only of the spatial links. The indices i and j run only over spatial directions. Since the spatial Wilson flow is diffused only in three-dimensional space, its diffusion radius is given by $\mathcal{R}_d = \sqrt{6\tau}$. We will later show that this new smearing works well even for the glueball spectroscopy without over smearing.

III. CALCULATION METHOD II: GLUEBALL TWO-POINT FUNCTION

We are interested in three lowest-lying glueball states, which carry specific quantum numbers, $J^{PC} = 0^{++}$ (scalar), 0^{-+} (pseudoscalar), or 2^{++} (tensor), in this study. In this section, we briefly describe how to construct two-point correlation functions of the desired glueball state having spin J , parity P , and charge-conjugation parity C .

First of all, on the lattice, rotational symmetry is reduced to the octahedral point group O , which is a finite subgroup of the rotation group $SO(3)$. There are 24 rotational operations associated with all proper rotations in the group O . The irreducible representations (irreps) R of O are the counterparts of spin J for the continuum rotation group $SO(3)$. There are five irreps, which are classified by two one-dimensional representations (denoted as A_1 and A_2), one two-dimensional representation (denoted as E), and two three-dimensional representations (denoted as T_1 and T_2) [13].

The inclusion of inversion (X is mapped to $-X$) results in the symmetry group known as O_h , which has $48 (= 24 \times 2)$ symmetry operations. The irreducible representations of O_h are obtained from those of O by appending the index g (gerade) or u (ungerade), which indicates even or odd parity [14]. For convenience, we use the indices $+$ and $-$, instead of g and u . Therefore, ten different irreducible representations of O_h are denoted as R^P , hereafter. The glueball states are also eigenstates of charge conjugation. Therefore, the quantum number of the lattice glueball state is specified by R^{PC} . The quantum number R^{PC} is expected to have the following correspondence: $0^{++} \leftrightarrow A_1^{++}$, $0^{-+} \leftrightarrow A_1^{-+}$ and $2^{++} \leftrightarrow E^{++} \oplus T_2^{++}$ in the continuum limit [13,14].

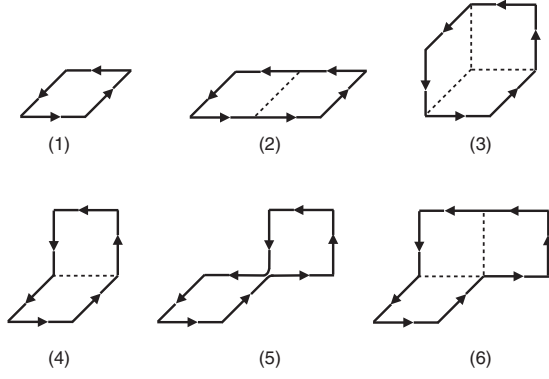


FIG. 1. Six prototypes of spacelike Wilson loops used to construct the glueball operators: (1) plaquette operator (denoted as $\mathcal{O}_{\text{plaq}}$), (2) rectangle operator (denoted as $\mathcal{O}_{\text{rect}}$), (3) twist operator (denoted as $\mathcal{O}_{\text{twist}}$), (4) chair operator (denoted as $\mathcal{O}_{\text{chair}}$), (5) “fish-shaped” operator (denoted as $\mathcal{O}_{\text{fish}}$), and (6) “hand-shaped” operator (denoted as $\mathcal{O}_{\text{hand}}$).

A. Glueball operators

We use six prototypes of spacelike Wilson loops to construct the glueball operators for four specific channels of $R^{PC} = A_1^{++}, A_1^{-+}, E^{++}$ and T_2^{++} as depicted in Fig. 1. First four operators are all types of spacelike Wilson loops with four and six links, while the remaining two operators are chosen from spacelike Wilson loops of eight links. Each operator \mathcal{O}_k is classified with the numbers of the links (denoted as l) involved in the Wilson loop, the shape characterized by the ordered closed path \mathcal{C}_k and the associated orientation as listed in Table I. In the case of $SU(N)$ with $N \geq 3$, the real part of Wilson loops has a charge conjugation parity $C = +1$, while the imaginary part has C -parity $C = -1$ [14]. In this study, we restrict ourselves to consider the real part of Wilson loops, since the three lowest-lying glueball states carry $C = +1$.

We take the following procedure to get the irreducible contents of the representation R^P with fixed C -parity from the operators \mathcal{O}_k according to Ref. [14]. First, 48 symmetry operations \hat{S}_i , which are defined in Table II, are applied to

each prototype of Wilson loops $\mathcal{O}_k[\mathcal{C}_k]$ so as to obtain 48 copies with different orientations of Wilson loops $\mathcal{O}_k[\hat{S}_i\mathcal{C}_k]$. A linear combination of them with weights equal to the irreducible characters $\chi_\Gamma(S_i)$ of S_i for the Γ irreps provides the operator projected onto the Γ irrep as

$$\mathcal{O}_k^\Gamma = \hat{P}_\Gamma \mathcal{O}_k[\mathcal{C}_k] = \frac{1}{48} \sum_{i=1}^{48} \chi_\Gamma^*(S_i) \mathcal{O}_k[\hat{S}_i\mathcal{C}_k], \quad (5)$$

where the characters $\chi_\Gamma(S_i)$ of the irreps $\Gamma = A_1^+, A_1^-, E^+$ and T_2^+ are listed in Table III.

We next construct two-point correlation functions of glueball states for given irreps Γ as

$$C_k^\Gamma(t) = \sum_{t'} \langle 0 | \tilde{\mathcal{O}}_k^\Gamma(t+t') \tilde{\mathcal{O}}_k^\Gamma(t')^\dagger | 0 \rangle, \quad (6)$$

where the tilde over \mathcal{O}_k^Γ implies the vacuum-subtracted operator defined as $\tilde{\mathcal{O}}_k^\Gamma(t) = \mathcal{O}_k^\Gamma(t) - \langle 0 | \mathcal{O}_k^\Gamma(t) | 0 \rangle$. We may also consider an $N \times N$ correlation matrix using a set of different shape operators for given irreps Γ [15] as

$$C_{kk'}^\Gamma(t) = \sum_{t'} \langle 0 | \tilde{\mathcal{O}}_k^\Gamma(t+t') \tilde{\mathcal{O}}_{k'}^\Gamma(t')^\dagger | 0 \rangle, \quad (7)$$

which allow us to perform the variational method [16,17].

IV. LATTICE SETUP

A. Gauge ensembles

We perform the pure Yang-Mills lattice simulations using the standard Wilson plaquette action with a fixed physical volume ($La \approx 1.6$ fm) at four different gauge couplings ($\beta = 6/g_0^2 = 6.2, 6.4, 6.71, \text{ and } 6.93$). The gauge configurations in each simulation are separated by n_{update} sweeps after n_{therm} sweeps for thermalization as summarized in Table IV. Each sweep consists of one heat bath [18] combined with four over-relaxation [19] steps. The number of configurations analyzed is $\mathcal{O}(500\text{--}4000)$.

TABLE I. Classification of spacelike Wilson loops used in this study. Each operator \mathcal{O}_k is classified with the shape (labeled as k) characterized by the ordered closed path (denoted as \mathcal{C}_k) and the numbers of the links (denoted as l) involved in the Wilson loop. In the table, the paths for prototype of Wilson loops depicted in Fig. 1 are given with an l -tuple composed of the direction of the coordinate axes as $\pm X, \pm Y$, and $\pm Z$. The minus sign indicates the path along in the negative direction. The check mark symbol (\checkmark) in the table indicates that the operator contains the corresponding irreducible representation [14].

Label k	No. of links l	Prototype path \mathcal{C}_k	Target irreps			
			A_1^{++}	A_1^{-+}	E^{++}	T_2^{++}
Plaq	4	$[X, Y, -X, -Y]$	\checkmark		\checkmark	
Rect	6	$[X, X, Y, -X, -X, -Y]$	\checkmark		\checkmark	
Twist	6	$[X, Y, Z, -X, -Y, -Z]$	\checkmark			\checkmark
Chair	6	$[X, Y, Z, -X, -Z, -Y]$	\checkmark		\checkmark	\checkmark
Fish	8	$[X, Y, X, Z, -X, -Z, -X, -Y]$	\checkmark	\checkmark	\checkmark	\checkmark
Hand	8	$[X, Y, X, Z, -X, -X, -Z, -Y]$	\checkmark	\checkmark	\checkmark	\checkmark

TABLE II. Each of 48 elements S_i of the group O_h , which are presented by the coordinate transformations, is divided into ten different conjugacy classes $\{E, 3C_4^2, 6C_4, 8C_3, 6C_2', I, 3\sigma_h, 6IC_4, 8IC_3, 6\sigma_d\} \in O_h$.

Class	i	Operation	Class	i	Operation
E	1	$(X, Y, Z) \rightarrow (X, Y, Z)$	I	25	$(X, Y, Z) \rightarrow (-X, -Y, -Z)$
$3C_4^2$	2	$(X, Y, Z) \rightarrow (-X, -Y, Z)$	$3\sigma_h$	26	$(X, Y, Z) \rightarrow (X, Y, -Z)$
	3	$(X, Y, Z) \rightarrow (-X, Y, -Z)$		27	$(X, Y, Z) \rightarrow (X, -Y, Z)$
	4	$(X, Y, Z) \rightarrow (X, -Y, -Z)$		28	$(X, Y, Z) \rightarrow (-X, Y, Z)$
$6C_4$	5	$(X, Y, Z) \rightarrow (-Y, X, Z)$		$6IC_4$	29
	6	$(X, Y, Z) \rightarrow (Y, -X, Z)$	30		$(X, Y, Z) \rightarrow (-Y, X, -Z)$
	7	$(X, Y, Z) \rightarrow (Z, Y, -X)$	31		$(X, Y, Z) \rightarrow (-Z, -Y, X)$
	8	$(X, Y, Z) \rightarrow (-Z, Y, X)$	32		$(X, Y, Z) \rightarrow (Z, -Y, -X)$
	9	$(X, Y, Z) \rightarrow (X, -Z, Y)$	33		$(X, Y, Z) \rightarrow (-X, Z, -Y)$
	10	$(X, Y, Z) \rightarrow (X, Z, -Y)$	34		$(X, Y, Z) \rightarrow (-X, -Z, Y)$
$8C_3$	11	$(X, Y, Z) \rightarrow (Y, Z, X)$	$8IC_3$	35	$(X, Y, Z) \rightarrow (-Y, -Z, -X)$
	12	$(X, Y, Z) \rightarrow (Z, X, Y)$		36	$(X, Y, Z) \rightarrow (-Z, -X, -Y)$
	13	$(X, Y, Z) \rightarrow (Y, -Z, -X)$		37	$(X, Y, Z) \rightarrow (-Y, Z, X)$
	14	$(X, Y, Z) \rightarrow (-Z, -X, Y)$		38	$(X, Y, Z) \rightarrow (Z, X, -Y)$
	15	$(X, Y, Z) \rightarrow (-Y, Z, -X)$		39	$(X, Y, Z) \rightarrow (Y, -Z, X)$
	16	$(X, Y, Z) \rightarrow (Z, -X, -Y)$		40	$(X, Y, Z) \rightarrow (-Z, X, Y)$
	17	$(X, Y, Z) \rightarrow (-Y, -Z, X)$		41	$(X, Y, Z) \rightarrow (Y, Z, -X)$
	18	$(X, Y, Z) \rightarrow (-Z, X, -Y)$		42	$(X, Y, Z) \rightarrow (Z, -X, Y)$
$6C_2'$	19	$(X, Y, Z) \rightarrow (Y, X, -Z)$	$6\sigma_d$	43	$(X, Y, Z) \rightarrow (-Y, -X, Z)$
	20	$(X, Y, Z) \rightarrow (Z, -Y, X)$		44	$(X, Y, Z) \rightarrow (-Z, Y, -X)$
	21	$(X, Y, Z) \rightarrow (-X, Z, Y)$		45	$(X, Y, Z) \rightarrow (X, -Z, -Y)$
	22	$(X, Y, Z) \rightarrow (-Y, -X, -Z)$		46	$(X, Y, Z) \rightarrow (Y, X, Z)$
	23	$(X, Y, Z) \rightarrow (-Z, -Y, -X)$		47	$(X, Y, Z) \rightarrow (Z, Y, X)$
	24	$(X, Y, Z) \rightarrow (-X, -Z, -Y)$		48	$(X, Y, Z) \rightarrow (X, Z, Y)$

TABLE III. Table of characters $\chi_\Gamma(S_i)$ for four irreps, A_1^+ , A_1^- , E^+ , and T_2^+ of the group O_h . The elements S_i of the group O_h belong to ten different conjugacy classes $\{E, 3C_4^2, 6C_4, 8C_3, 6C_2', I, 3\sigma_h, 6IC_4, 8IC_3, 6\sigma_d\}$ [14].

Irreps	E	$3C_4^2$	$6C_4$	$8C_3$	$6C_2'$	I	$3\sigma_h$	$6IC_4$	$8IC_3$	$6\sigma_d$
A_1^+	+1	+1	+1	+1	+1	+1	+1	+1	+1	+1
A_1^-	+1	+1	+1	+1	+1	-1	-1	-1	-1	-1
E^+	+2	+2	0	-1	0	+2	+2	0	-1	0
T_2^+	+3	-1	-1	0	+1	+3	-1	-1	0	+1

TABLE IV. Summary of the gauge ensembles: gauge coupling, lattice size ($L^3 \times T$), plaquette value, lattice spacing (a), spatial extent (La), the Sommer scale (r_0), the number of the gauge field configurations (N_{conf}), the number of thermalization sweeps (n_{therm}) and the number of update sweeps (n_{update}). All lattice spacings are set by the Sommer scale ($r_0 = 0.5$ fm) [20,21].

$\beta = 6/g_0^2$	$L^3 \times T$	plaquette	a [fm]	$\sim La$ [fm]	r_0/a (Ref. [21])	N_{conf}	n_{therm}	n_{update}
6.20	$24^3 \times 24$	0.613644(3)	0.0677(3)	1.62	7.38(3)	4000	5000	200
6.40	$32^3 \times 32$	0.630646(2)	0.0513(3)	1.64	9.74(5)	3000	5000	200
6.71	$48^3 \times 48$	0.653298(2)	0.0345(2)	1.66	14.49(10)	1000	25000	200
6.93	$64^3 \times 64$	0.667376(1)	0.0256(2)	1.64	19.48(12)	500	64000	600

All lattice spacings are set by the Sommer scale ($r_0 = 0.5$ fm) [20,21].

For both original and spatial gradient flows, the fourth-order Runge-Kutta scheme is used with an integration step size of $\epsilon = 0.025$. The flow time τ is given by $n_{\text{flow}} \times \epsilon$

where n_{flow} denotes the number of flow iterations. Our simulation code for the gradient flow had been already checked in Table II of Ref. [22], where the values of the gradient flow reference scale are directly compared with the results given in the original work of Lüscher [9].

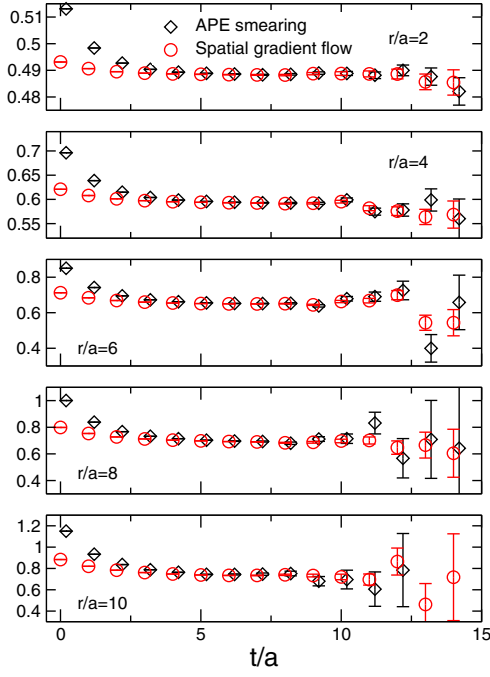


FIG. 2. The t -dependence of $V(r, t)$ for several values of fixed r/a ($r/a = 2, 4, 6, 8, 10$ from top panel to bottom panel). The Wilson loops $W(r, t)$ are constructed by the smeared spatial links, which are computed with either APE smearing (diamonds) or spatial gradient flow (circles). The spatial gradient flow provides longer plateau behaviors than those of APE smearing.

B. Scale setting and static quark potential

The static potential $V(r)$ between heavy quark and antiquark pairs, which are separated by relative distance r , is calculated from the Wilson-loop expectation value $\langle W(r, t) \rangle$ with spatial extent r and temporal extent t as

$$\langle W(r, t) \rangle = C(r)e^{-V(r)t} + \dots, \quad (8)$$

where the ellipsis denotes some contribution from the excited states.

To determine the static quark potential $V(r)$, let us consider the following quantity:

$$V(r, t) = \ln \left\{ \frac{\langle W(r, t) \rangle}{\langle W(r, t+1) \rangle} \right\}. \quad (9)$$

Since the t -dependence of $V(r, t)$ is expected to disappear for sufficiently large t , the static potential $V(r)$ can be determined from a plateau seen in $V(r, t)$ as t increases for fixed r .

Figure 2 shows the t -dependence of $V(r, t)$ calculated at $\beta = 6.4$ for fixed r/a ($r/a = 2, 4, 6, 8, 10$ from top panel to bottom panel) as typical examples. The Wilson loops $W(r, t)$ are constructed by the smeared spatial links, which are computed with either APE smearing or spatial gradient

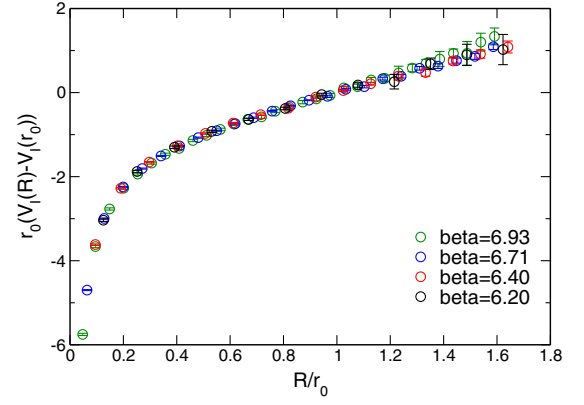


FIG. 3. The lattice spacing dependence of $V_I(R)$. The vertical and horizontal axes are normalized by the Sommer scale r_0 given in Ref. [21]. For clarity of the figure, a constant shift has been applied by subtraction of the value at $R = r_0$.

flow. The diamond symbols represent the results calculated using APE smearing with $\alpha_{\text{APE}} = 0.5$ and 5 steps, while the circle symbols represent the results calculated using spatial gradient flow with $n_{\text{flow}} = 50$.

At glance, spatial gradient flow provides the better behavior, where the plateau starts at earlier t and extends to larger t , comparing with APE smearing. It indicates that the systematic uncertainties stemming from the excited-state contamination are better under control to determine the static potential using the spatial gradient flow method.

Hereafter, we adopt the spatial gradient flow method to evaluate the value of $V(r)$ from the Wilson-loop expectation value, and then aim to determine the Sommer scale from the resulting static potential at each β . In this study, the Wilson loops are restricted to on-axis loops only. To extract the value of $V(r)$ from $\langle W(r, t) \rangle$ at fixed r , we use the double-exponential fit, where the correlation among $\langle W(r, t) \rangle$ at different value of t is taken into account by using a covariance matrix, for our final analysis. To apply a tree-level improvement on the static quark potential, we consider

$$V_I(R) = V(r) \quad (10)$$

with $(4\pi R)^{-1} = G(r, 0, 0)$ where $G(\mathbf{r})$ is the (scalar) lattice propagator in three dimensions [21].

In Fig. 3, all data points of $V_I(R)$, which are computed at four different lattice spacings, are plotted as a function of R . The vertical and horizontal axes are normalized by the Sommer scale r_0 given in Ref. [21]. For clarity of the figure, the self-energy contribution is subtracted by the value at $R = r_0$. Our results of $V_I(R)$ obtained by spatial gradient flow exhibit good scaling behavior with the literature values of r_0/a [21]. We finally determine r_0 from our results of the static quark potentials computed at four gauge

TABLE V. Summary of the Cornell potential parameters (V_0 , A , and $\sqrt{\sigma}$) and the Sommer parameter r_0 in lattice units for all four ensembles.

β	aV_0	A	$a\sqrt{\sigma}$	r_0/a	$[r_{\min}/a, r_{\max}/a]$	χ^2/dof
6.2	0.623(7)	0.257(9)	0.1647(38)	7.16(15)	[2, 9]	1.02
6.4	0.606(9)	0.284(26)	0.1220(32)	9.58(17)	[4, 13]	0.81
6.71	0.569(13)	0.331(65)	0.0819(39)	14.02(33)	[8, 16]	1.15
6.93	0.541(8)	0.339(43)	0.0608(29)	18.84(61)	[8, 21]	0.98

couplings. For this purpose, we first adopt the Cornell potential parametrization by fitting the data of $V_I(R)$ as

$$V_I(R) = V_0 - \frac{A}{R} + \sigma R \quad (11)$$

with the Coulombic coefficient A , the string tension σ , and a constant V_0 . Finally, the parameters A and σ can be used to determine the Sommer scale r_0 as

$$r_0 = \sqrt{\frac{1.65 - A}{\sigma}} \quad (12)$$

for each gauge coupling β . In Table V, we summarize the fit results of the Cornell potential parameters (V_0 , A , and $\sqrt{\sigma}$) and the Sommer parameter r_0 obtained from all four ensembles, in lattice units. Although all measured values of the Sommer parameter are barely consistent with the literature values of r_0/a [21], while our estimates of r_0/a are systematically underestimated.

The origin for the underestimation of r_0/a is twofold. According to Eq. (12), one is the overestimation of A , while the other is the overestimation of σ . In the string regime ($R > 1$ fm) [23], the effective string theory predicts that the coefficient A is given by the universal Lüscher constant $A = \pi/12$ [24], which is smaller than our estimates of A . Thus, we alternatively choose fits with A fixed at $\pi/12$, though our data falls outside of this range. Nevertheless, the obtained results for the string tension σ becomes slightly larger than the values tabulated in Table V, so that the resulting values of r_0/a get smaller and go slightly further away from the literature values. We thus consider that the systematic underestimation of our values of r_0 is mainly caused by a slight overestimation of the string tension since the excited-state contaminations are not fully eliminated in our analysis of $V(r)$ especially for large r . We simply use the double-exponential fit to determine $V(r)$ from $\langle W(r, t) \rangle$ instead of the variational method that was adopted in Ref. [21].

Figure 3 shows the lattice spacing dependence of $V_I(R)$. The vertical and horizontal axes are normalized by the Sommer scale r_0 given in Ref. [21]. For clarity of the figure, a constant shift has been applied by subtraction of the value at $R = r_0$. Indeed, the scaling behavior, where the data points of $V_I(R)$ measured at different lattice spacings collapse on a single curve, is clearly seen in Fig. 3. We hereafter use the literature values of r_0/a [21] for whole analysis instead of our measured values.

V. FEATURES OF THE SPATIAL GRADIENT FLOW

A. Comparison with the original gradient flow

We first recapitulate the problem of a simple application of the original gradient flow to calculate the glueball two-point functions. In this subsection, we focus on the results of the A_1^{++} glueball state calculated on a 32^4 lattice at $\beta = 6.4$ with the “plaquette” glueball operator $\mathcal{O}_{\text{plaq}}$ as a typical example. In Fig. 4, we show the results of two-point functions (left panel) and their effective mass plots (right panel) using the original gradient flow with three values of flow time τ , which are represented by the values of the diffusion radius $R_d = \sqrt{8\tau}$ in lattice units.

As shown in the left panel of Fig. 4, the statistical errors on the glueball two-point function are dramatically reduced up to the large time slice region as the flow time increases. However, the temporal correlation in the region of $t < R_d$ become suffered from the overlap of two glueball operators which are smeared in space-time according to a Gaussian spread. In fact that if the two-point function $C(t)$ forms a Gaussian shape, $C(t) \propto C_{\text{gauss}}(t) = e^{-t^2/(2R_d^2)}$, with a Gaussian width corresponding to the diffusion radius R_d , its effective mass gives rise to a peculiar t -dependence as

$$M_{\text{eff}}(t') = \ln \left\{ \frac{C(t)}{C(t+1)} \right\} \approx \frac{t'}{R_d^2}, \quad (13)$$

whose value linearly increases from zero with a coefficient of $1/R_d^2$ as a function of the time slice $t' = t + \frac{1}{2}$. This feature can be observed in the right panel of Fig. 4, where each effective mass¹ approximately starts from zero and linearly raise up to around $t \approx R_d$ with increasing of the time slice t . Furthermore, as expected in Eq. (13), it is easily observed that the slope of the linear dependence decreases with the larger flow time. When the shorter flow time such as the case of $R_d/a = 4.47$ is chosen to avoid over smearing, the effective mass shows a plateau behavior in the region of $t > R_d$. For the longer flow time such as the cases of $R_d/a = 7.75$ and 10.0, the plateau formation becomes uncertain because R_d approaches the vicinity of the temporal midpoint ($t/a = 16$), where the signals of the

¹To take into account “the wrap-around effect” due to the periodic boundary condition, the effective masses $M_{\text{eff}}(t')$ are given by a solution of $\frac{C(t)}{C(t+1)} = \frac{\cosh[M_{\text{eff}}(t')(t-T/2)]}{\cosh[M_{\text{eff}}(t')(t+1-T/2)]}$ in the right panels of Figs. 4 and 5.

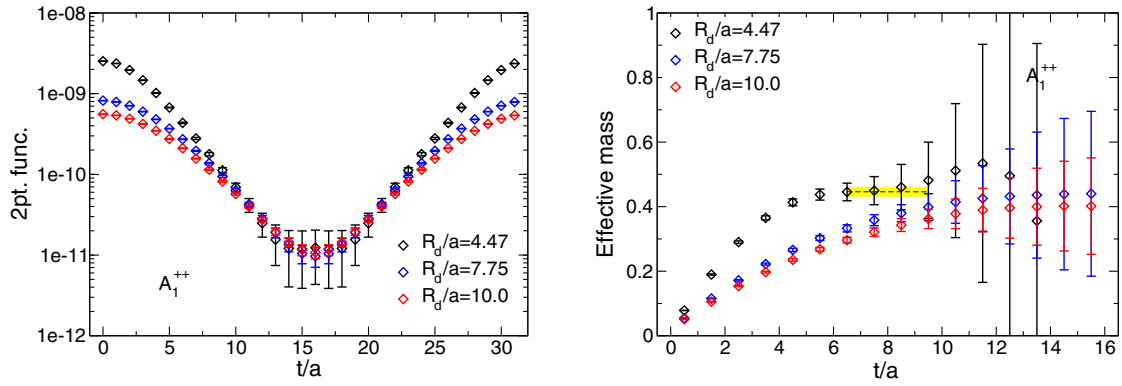


FIG. 4. Examples of the A_1^{++} glueball results obtained from the original gradient flow: two-point functions (left) and their effective mass plots (right) as functions of the time slice t for three values of flow time τ .

effective mass get noisier. As a result, the plateau behavior, which highly depends on the choice of the flow time, is too uncertain to extract the ground-state mass of the glueball with high accuracy.

We next show the results obtained from the spatial gradient flow in Fig. 5. First of all, in the left panel of Fig. 5, the exponential falloffs are clearly seen for all three values of the flow time and their slopes in the asymptotic region are independent of the choice of the flow time. The latter point can be confirmed in the right panel of Fig. 5, where their effective mass plots are displayed. For sufficiently large flow time ($\mathcal{R}_d/a > 6.71$), the plateau behavior in the effective mass plot does not change with variation in flow time. This is a great advantage compared to the original gradient flow. Furthermore, the plateau behavior starts at a smaller time slice, where the true temporal correlation of the glueball two-point function is kept unaffected during the smearing procedure contrast to the original gradient flow. It is another advantage for extracting the ground-state mass of the glueball with high accuracy, though the large statistical fluctuations still remain in the large t region.

Finally, we calculate the ground-state mass of the A_1^{++} glueball by fitting the glueball two-point function with a

single exponential form for both gradient flow cases. The choice of $\mathcal{R}_d/a = 4.47$ for the original gradient flow is taken to avoid over smearing, while the data with $\mathcal{R}_d/a = 8.66$ is used for the spatial gradient flow as a typical example. The A_1^{++} glueball masses are respectively evaluated from two types of the gradient flow as below,

$$aM_{A_1^{++}} = \begin{cases} 0.446(14) & \text{(original gradient flow)} \\ 0.404(9) & \text{(spatial gradient flow)}. \end{cases} \quad (14)$$

In the right panel of Figs. 4 and 5, each of the central values and errors is displayed as a blue dotted line and yellow shaded bands within the fit range. The statistical error on the original gradient flow result is slightly larger than that of the spatial gradient flow, while the central value of the former is slightly overestimated in comparison to the latter. Recall that the central value of the original gradient flow result tends to be lower when the flow time is taken longer regardless of over smearing. Needless to say, the original gradient flow requires the optimal choice of the flow time, while the spatial gradient flow result becomes stable for the large flow time.

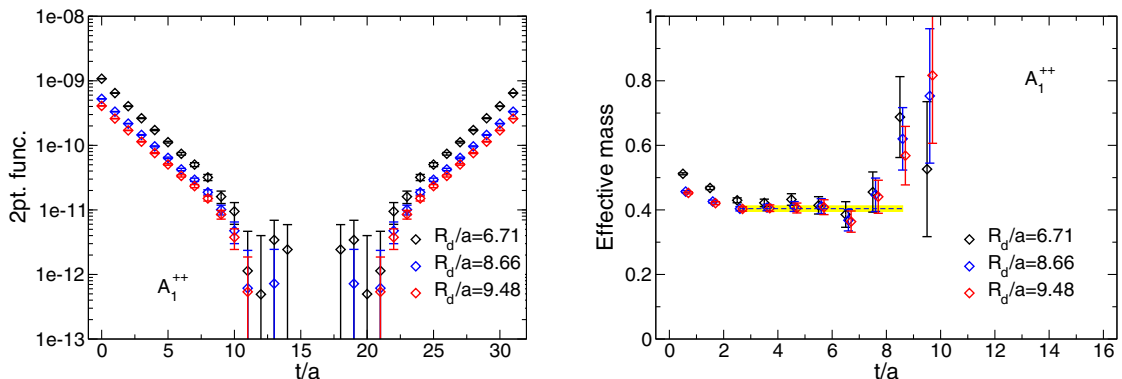


FIG. 5. Examples of the A_1^{++} glueball results obtained from the spatial gradient flow: two-point functions (left) and their effective mass plots (right) as functions of the time slice t for three values of flow time τ .

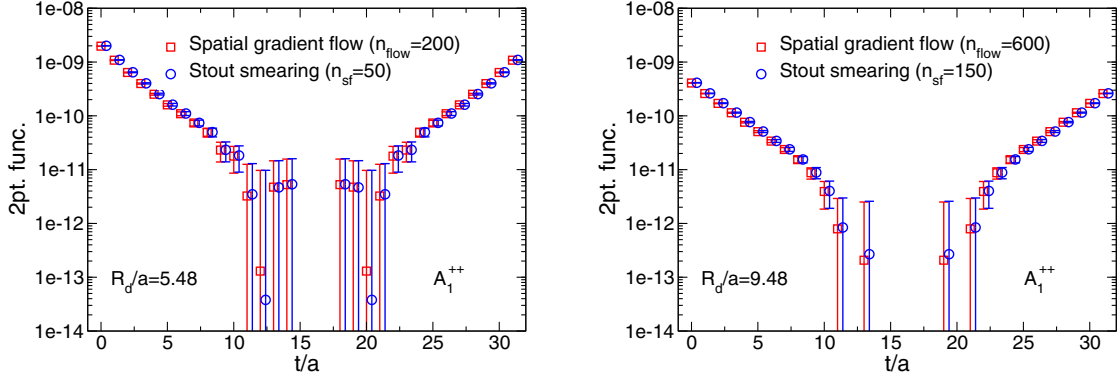


FIG. 6. Comparisons of the two-point functions for the A_1^{++} glueball using the spatial gradient flow and the stout smearing. The left panel is for the lower-diffusion case ($\mathcal{R}_d/a = 5.48$), while the right panel is for the higher-diffusion case ($\mathcal{R}_d/a = 9.48$).

As will be discussed in Appendix A, the spatial gradient flow is slightly more efficient than the gradient flow, which is diffused in the four-dimensional space-time, in terms of reduction of relative uncertainties. As reported in an earlier work [25], although the cooling method that can smoothen the whole four-dimensional space-time was also used for calculating the string tension and glueball masses, the similar conclusion is made that the results were not better than the conventional approach that can smoothen only the three-dimensional space.

B. Equivalence to the stout smearing

We will later show numerical equivalence between the spatial gradient flow and the stout smearing in the glueball calculations. As emphasized in Ref. [3], the stout smearing is a relatively new type of smearing technique, which can keep the differentiability with respect to the link variables during the smearing procedure. This property is maintained by the use of the exponential function in the stout-link smearing algorithm to remain within the $SU(3)$ group. For the gradient flow, the numerical integrations of Eqs. (2) and (3) with respect to the flow time are performed with the Runge-Kutta scheme to obtain the Wilson flow as a solution of

Eqs. (2) and (3). This procedure requires the exponentiation of the “Lie-algebra fields” for the integration. In this sense, neither of the two methods uses the projection into $SU(3)$ for the flowed or smeared link variables.

The gradient flow equation can be regarded as a continuous version of the recursive update procedure in the stout-link smearing as pointed out in the original paper [9]. Moreover, the authors of Ref. [10] relate the smoothing parameter for other smearing schemes to the gradient flow time τ under the assumption that the lattice spacing and the smearing parameters are small enough. For the case of the stout smearing, the corresponding flow time τ is given by the matching relation of $\tau = \rho n_{st}$ with the number of stout smearing steps n_{st} for the isotropic four-dimensional case of the stout smearing parameters ($\rho_{\mu\nu} = \rho$) [10]. We will later rederive the above matching relation in more rigorous manner in Appendix A.

In Fig. 7, we show the effective masses of the A_1^{++} glueball state obtained from the spatial gradient flow and the stout smearing at the same flow time τ that is determined by the matching relation, $\tau = \rho n_{st}$, between the two methods. In this work, for the stout smearing, the spatially isotropic three-dimensional parameter set is chosen to be $\rho_{ij} = \rho = 0.1$ and $\rho_{4\mu} = \rho_{\mu 4} = 0$. The numerical

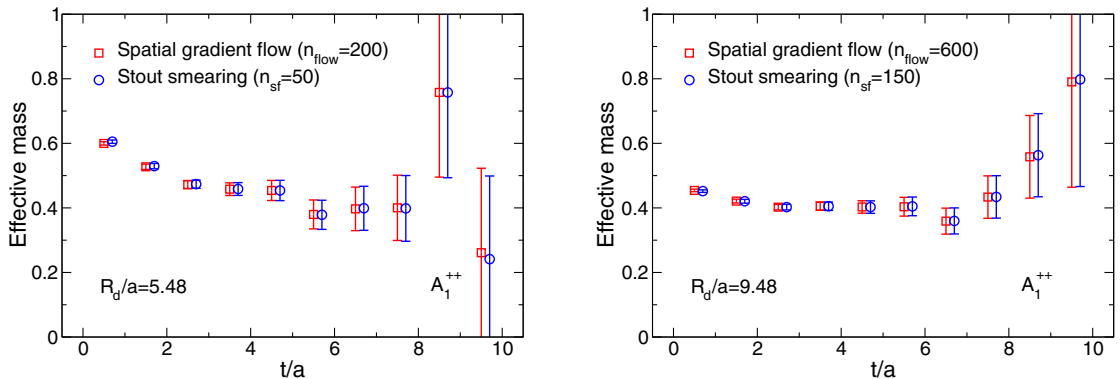


FIG. 7. Comparisons of the effective mass plots for the A_1^{++} glueball using the spatial gradient flow and the stout smearing. The left panel is for the lower-diffusion case ($\mathcal{R}_d/a = 5.48$), while the right panel is for the higher-diffusion case ($\mathcal{R}_d/a = 9.48$).

TABLE VI. Summary of glueball simulation parameters: gauge coupling, lattice size ($L^3 \times T$), the number of the accumulated gauge configurations (N_{conf}), the number of measurements per configuration (N_{meas}), the number of total measurements ($N_{\text{total}} = N_{\text{conf}} \times N_{\text{meas}}$) and the number of flow iterations (n_{flow}).

β	$L^3 \times T$	N_{conf}	N_{meas}	N_{total}	n_{flow}
6.2	$24^3 \times 24$	4000	4	16000	From 50 to 500 (every 50)
6.4	$32^3 \times 24$	3000	4	12000	From 50 to 800 (every 50)
6.71	$48^3 \times 48$	1000	4	4000	From 50 to 1400 (every 50)
6.93	$64^3 \times 64$	500	4	2000	From 50 to 2600 (every 50)

equivalence between the two methods is clearly observed in both the lower and higher-diffusion cases as shown in Fig. 6. It is worth remarking that the values of n_{st} adopted in Fig. 7, is much larger than a typical value of less than ten in the usual usage. Although the usage of the stout smearing with a small value of n_{st} is not effective for the glueball calculations, the almost identical result to the one made by the spatial gradient flow with the diffusion radius ($\sqrt{6\tau}$) can be obtained by the case if the same amount of the diffusion radius ($\sqrt{6\rho n_{\text{st}}}$) is adopted in the stout smearing.

VI. RESULTS

In this section, we present the results of glueball masses in the four channels (A_1^{++} , A_1^{-+} , E^{++} , and T_2^{++}) using the spatial gradient flow. To perform the continuum

extrapolation, we calculate the glueball masses at four different gauge couplings with a fixed physical volume ($La \approx 1.6$ fm). In this section, we rotate the temporal direction using hypercubic symmetry of each gauge configuration and then increase the total number of glueball mass measurements by a factor of four as listed in Table VI. The maximum number of flow iterations corresponds to the diffusion radius $\mathcal{R}_d \approx 0.5\text{--}0.6$ fm at each ensemble.

A. Less shape-dependence

As described in Sec. VB, in this study, we adopt six types of Wilson loop shapes (plaquette, rectangle, twist, chair, fish, hand) [15] to construct the glueball operators. In the largest case, the A_1^{++} glueball state can be created with all six operators, and even in the smallest case, at least two

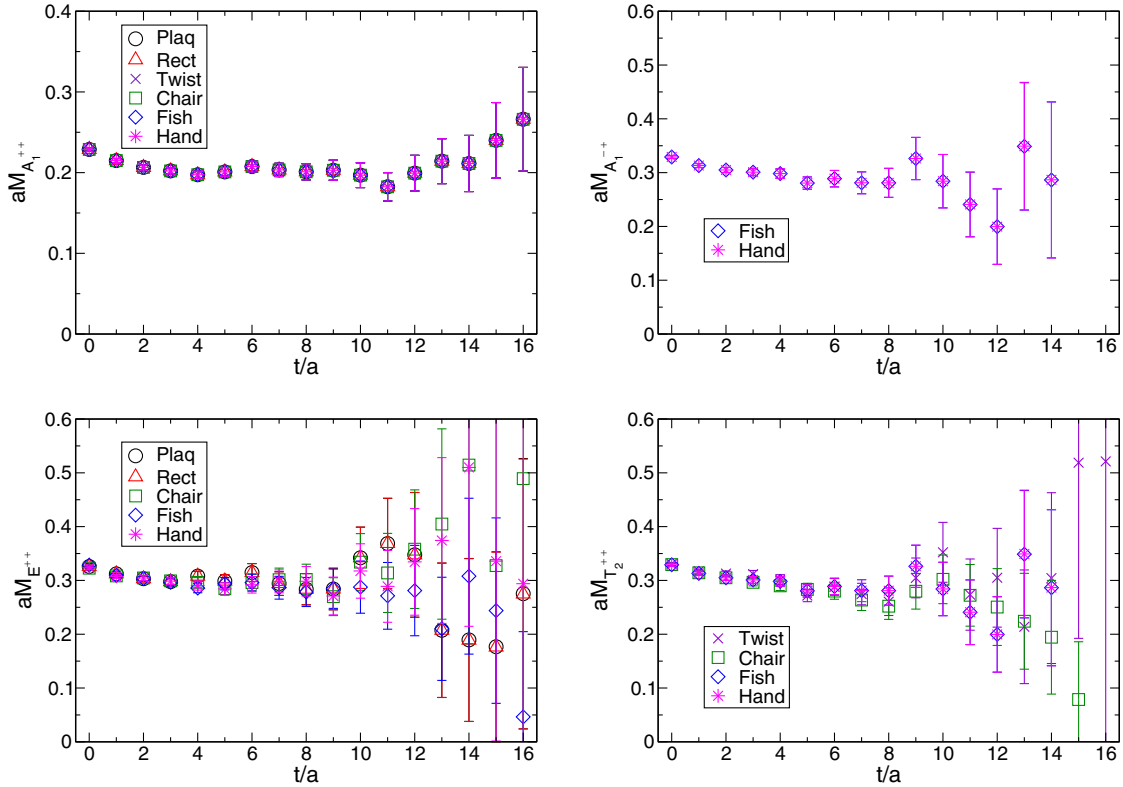


FIG. 8. Operator shape-dependence of effective masses with A_1^{++} (top-left), A_1^{-+} (top-right), E^{++} (bottom-left), and T_2^{++} (bottom-right) irreps. at $\beta = 6.93$ with $n_{\text{flow}} = 2000$ ($\mathcal{R}_d \approx 0.44$ fm).

operators can be used to compute the A_1^{-+} glueball state as summarized in Table I. In this sense, the variational analysis [16,17] based on the different shapes is in principle applicable, according to Ref. [15]. However, it is found that the shape-dependence of the resulting two-point functions disappears due to a strong isotropic nature in the spatial gradient flow method as shown in Fig. 8. These figures are displayed as typical examples.

The top panels of Fig. 8 show the effective mass plots for the A_1^{++} (left) and A_1^{-+} (right) channels at $\beta = 6.93$ with $n_{\text{flow}} = 2000$ ($\mathcal{R}_d \approx 0.44$ fm). All data points of different symbols including their error bars overlap each other. As shown in the bottom panels of Fig. 8, some of different operators are almost identical (e.g., plaquette and rectangle operators for the E^{++} channel, and also fish and hand operators for the T_2^{++} channel), though all data points of the effective mass are almost similar at a smaller time slice even for the tensor cases.

It is worth remarking that both the spatial gradient flow and stout smearing methods share this strong isotropic nature in the extended glueball operators after the large flow time or the high-diffusion case. Therefore, the variational analysis [16,17] based on the different shapes is not applicable at the fixed flow time or the fixed smearing step. However, instead of the different shapes, we can use the different diffuseness of the extended operator, which is given at the different flow time or the different smearing step, to carry out the variational analysis.

B. Variational analysis

As described in the previous subsection, we perform the variational analysis [16,17] with a set of basis operators, which are made of the flowed link variables at the different flow time for a fixed shape k . In this study, we choose the “fish” shaped operator $\mathcal{O}_{\text{fish}}$ which contains all irreps of our target states (A_1^{++} , A_1^{-+} , E^{++} , T_2^{++}).

For the variational analysis, we construct the $N \times N$ correlation matrix of two-point functions of glueball states for given irreps Γ as

$$C_{\alpha\beta}^{\Gamma}(t) = \sum_{t'} \langle 0 | \tilde{\mathcal{O}}_{\alpha}^{\Gamma}(t+t') \tilde{\mathcal{O}}_{\beta}^{\Gamma}(t')^{\dagger} | 0 \rangle, \quad (15)$$

where the labels of α , β , which run from 1 to N , identify the different flow iterations. The tilde over $\mathcal{O}_{\alpha}^{\Gamma}$ indicates the vacuum-subtracted operator as $\tilde{\mathcal{O}}_{\alpha}^{\Gamma}(t) = \mathcal{O}_{\alpha}^{\Gamma}(t) - \langle 0 | \mathcal{O}_{\alpha}^{\Gamma}(t) | 0 \rangle$. We next solve the generalized eigenvalue problem,

$$C_{\alpha\beta}^{\Gamma}(t) \omega_{n,\beta} = \lambda_{n,\Gamma}(t, t_0) \omega_{n,\beta} \quad (16)$$

to obtain the n th eigenvalue $\lambda_{n,\Gamma}(t, t_0)$, where t_0 is a reference time slice, and its eigenvector $\omega_{n,\beta}$. If only the N lowest states are propagating in the region where $t \geq t_0$,

the n th eigenvalue $\lambda_{n,\Gamma}(t, t_0)$ for $n \leq N$ is given by a single exponential form with the rest mass of the n th glueball state as

$$\lambda_{n,\Gamma}(t, t_0) = e^{-(t-t_0)M_{n,\Gamma}}, \quad (17)$$

which corresponds to the eigenvalue of the transfer matrix between two time slices t and t_0 . Details of how to practically compute the eigenvalues $\lambda_{n,\Gamma}(t, t_0)$ are described in Appendix B of Ref. [26]. An effective mass is defined as

$$M_{n,\Gamma}^{\text{eff}}(t) = \ln \frac{\lambda_{n,\Gamma}(t, t_0)}{\lambda_{n,\Gamma}(t+1, t_0)}, \quad (18)$$

where $\lambda_{n,\Gamma}(t, t_0)$ is the n th eigenvalue of the $N \times N$ correlation matrix for $\Gamma = A_1^{++}$, A_1^{-+} , E^{++} , T_2^{++} . In this study, we choose $N = 6$ and the reference time slice as $t_0/a = 0$, where the resulting mass is less sensitive to variation of t_0 .

Let us first present the effective masses of glueballs obtained from the variational method using the 6×6 correlation matrix constructed by the $\mathcal{O}_{\text{fish}}$ operator with six different flow iterations. Figure 9 show the effective mass plots of the first two eigenvalues in the A_1^{++} (top-left), A_1^{-+} (top-right), E^{++} (bottom-left), and T_2^{++} (bottom-right) representations at $\beta = 6.20$. Figures 10–12 are also plotted for the results obtained at $\beta = 6.40$, 6.71, and 6.93, respectively. In each panel of these figures, the horizontal solid lines represent each fit result obtained by a correlated fit using a single-exponential functional form, and shaded bands display the fit range and one standard deviation. As can be seen, the variational analysis with the correlation matrix constructed in our chosen basis successfully separates the first excited state from the ground state in each channel. In Table VII, we summarize the results of masses of the two lowest-lying glueball states in all four channels, together with fit ranges used in the fits and value of χ^2 per degrees of freedom (dof).

C. Continuum extrapolation and comparison with previous results

It is worth comparing our result obtained from the spatial gradient flow with previous results obtained from both the original gradient flow and a conventional approach. For this purpose, we choose the results obtained in the simulations performed on isotropic lattice with the standard Wilson plaquette action. The previous attempt to apply the gradient flow to the A_1^{++} glueball spectroscopy was done by Chowdhury-Harindranath-Maiti [12] (denoted as CHJ result). Meyer [7] and Athenodorou-Teper [8] (denoted as AT result) performed comprehensive studies of the low-lying glueball states using the conventional approach at several lattice spacings.

In Fig. 13, we show our results of the ground-state glueball masses calculated in the A_1^{++} (top-left), A_1^{-+}

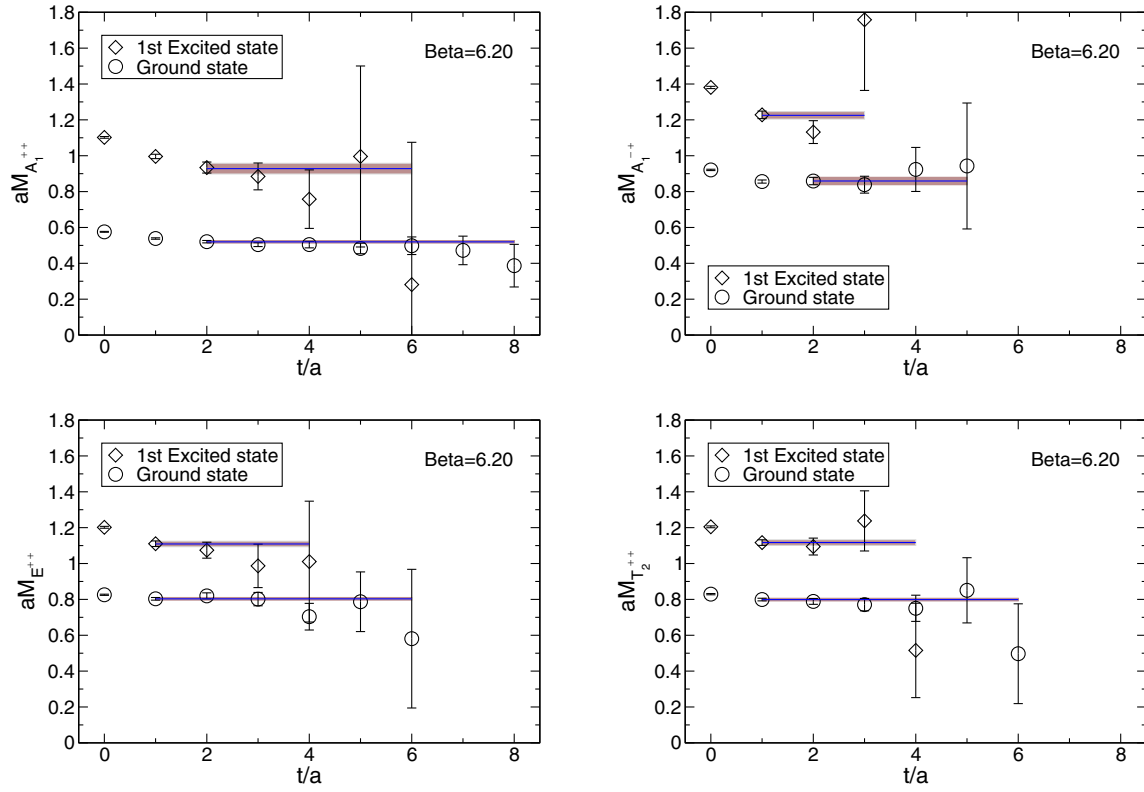


FIG. 9. Effective mass plots for the ground state and the first excited state in A_1^{++} (top-left), A_1^{+-} (top-right), E^{++} (bottom-left), and T_2^{++} (bottom-right) channels at $\beta = 6.20$.

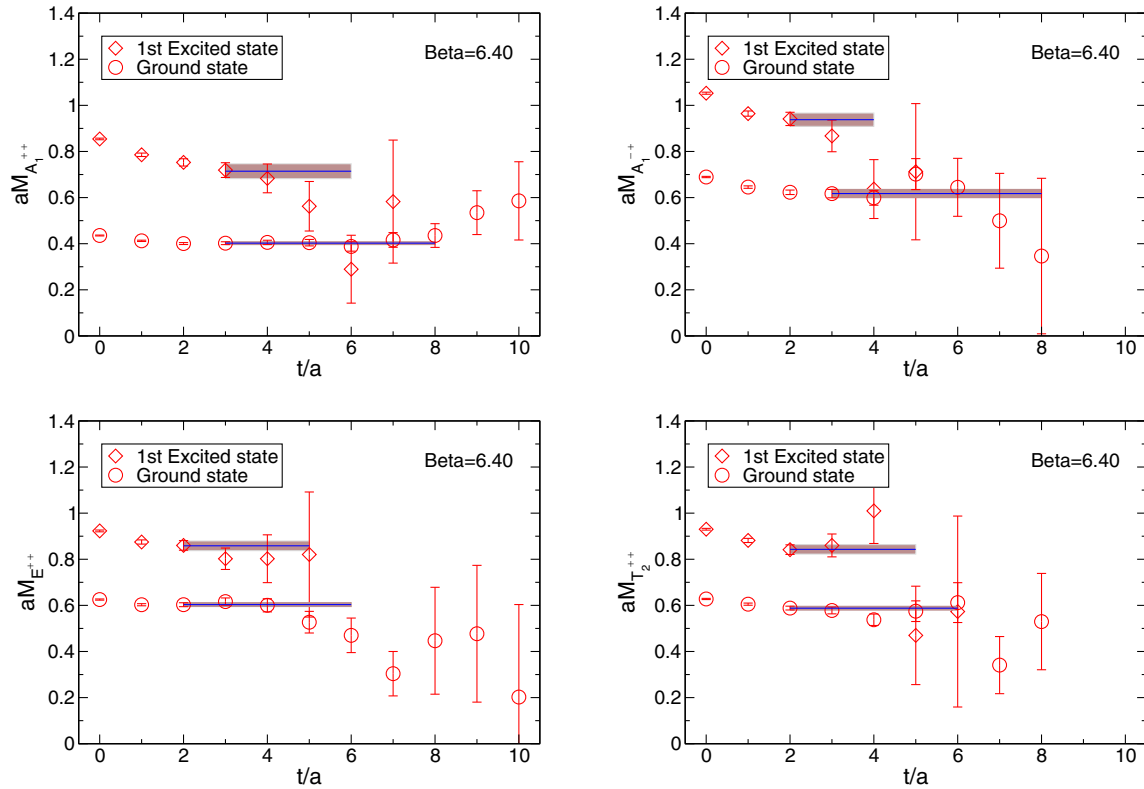


FIG. 10. Effective mass plots for the ground state and the first excited state in A_1^{++} (top-left), A_1^{+-} (top-right), E^{++} (bottom-left), and T_2^{++} (bottom-right) channels at $\beta = 6.40$.

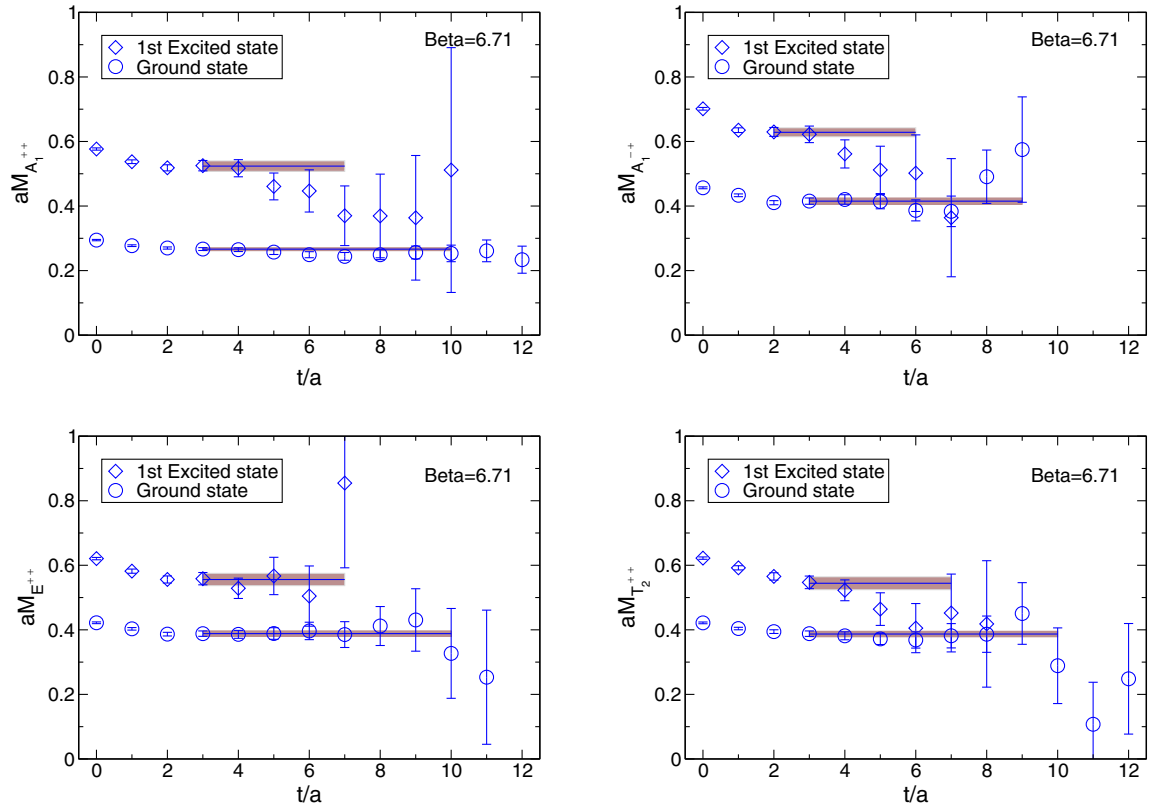


FIG. 11. Effective mass plots for the ground state and the first excited state in A_1^{++} (top-left), A_1^{+-} (top-right), E^{++} (bottom-left), and T_2^{++} (bottom-right) channels at $\beta = 6.71$.

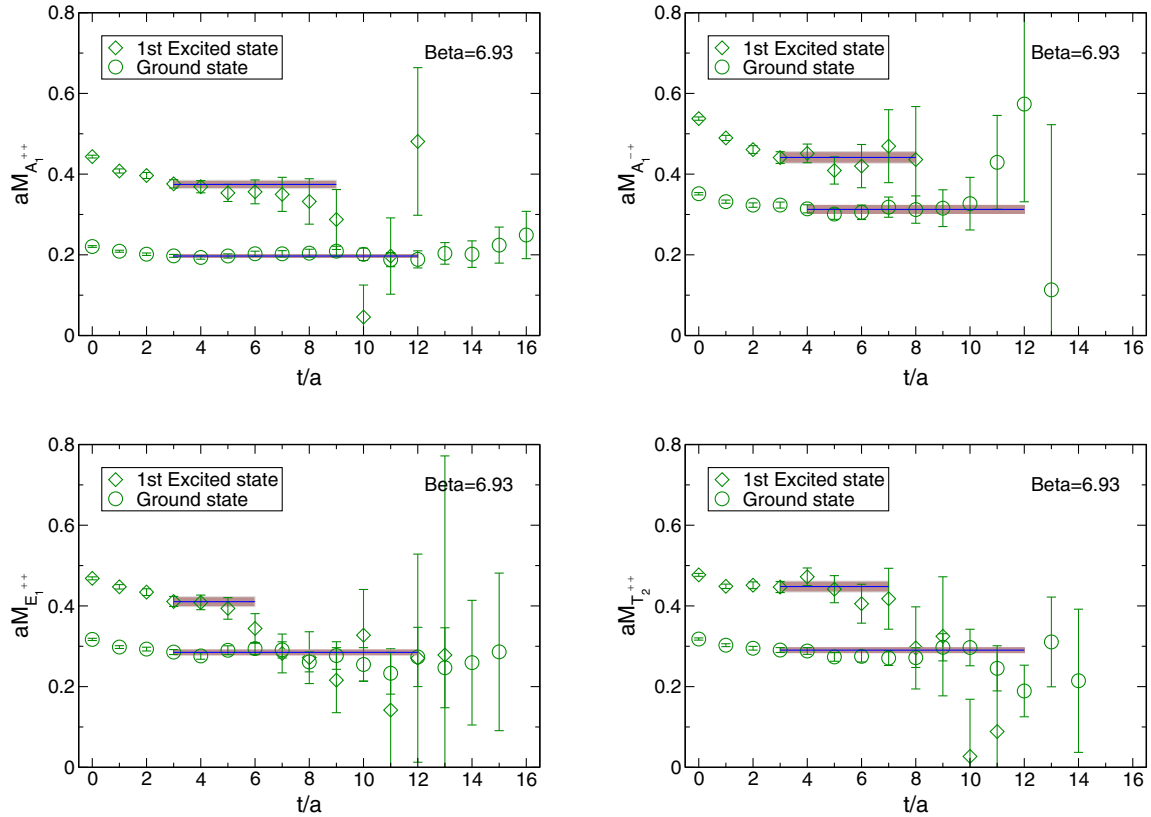


FIG. 12. Effective mass plots for the ground state and the first excited state in the A_1^{++} (top-left), A_1^{+-} (top-right), E^{++} (bottom-left), and T_2^{++} (bottom-right) channels at $\beta = 6.93$.

TABLE VII. Masses of the ground state and the first excited state of glueballs obtained from the variational method using the 6×6 correlation matrix constructed by the $\mathcal{O}_{\text{fish}}$ operator with six different flow iterations.

Irreps	β	Ground state			First excited-state		
		aM_G	Fit range	χ^2/dof	aM_G	Fit range	χ^2/dof
A_1^{++}	6.2	0.5198(67)	[2, 8]	0.82	0.928(30)	[2, 6]	0.42
	6.4	0.4025(62)	[3, 8]	0.61	0.714(32)	[3, 6]	0.89
	6.71	0.2664(45)	[3,10]	0.85	0.518(10)	[2, 6]	0.85
	6.93	0.1970(36)	[3,12]	0.98	0.374(10)	[3, 9]	0.30
E^{++}	6.2	0.8032(74)	[1, 6]	0.84	1.109(16)	[1, 4]	0.66
	6.4	0.6035(85)	[2, 6]	1.47	0.858(21)	[2, 5]	0.83
	6.71	0.3884(83)	[3,10]	0.12	0.556(19)	[3, 7]	0.66
	6.93	0.2849(61)	[3,12]	1.16	0.411(12)	[3, 6]	0.25
T_2^{++}	6.2	0.7989(74)	[1, 6]	0.31	1.117(16)	[1, 4]	0.47
	6.4	0.5878(84)	[2, 6]	1.58	0.843(21)	[2, 5]	0.90
	6.71	0.3871(85)	[3,10]	0.35	0.544(20)	[3, 7]	1.24
	6.93	0.2904(62)	[3,12]	0.81	0.448(14)	[3, 7]	1.36
A_1^{-+}	6.2	0.859(20)	[2, 5]	0.37	1.225(21)	[1, 3]	2.13
	6.4	0.618(18)	[3, 8]	1.04	0.938(29)	[2, 4]	1.14
	6.71	0.415(10)	[3, 9]	0.87	0.629(14)	[2, 6]	1.12
	6.93	0.313(10)	[4,12]	0.54	0.441(14)	[3, 8]	0.55

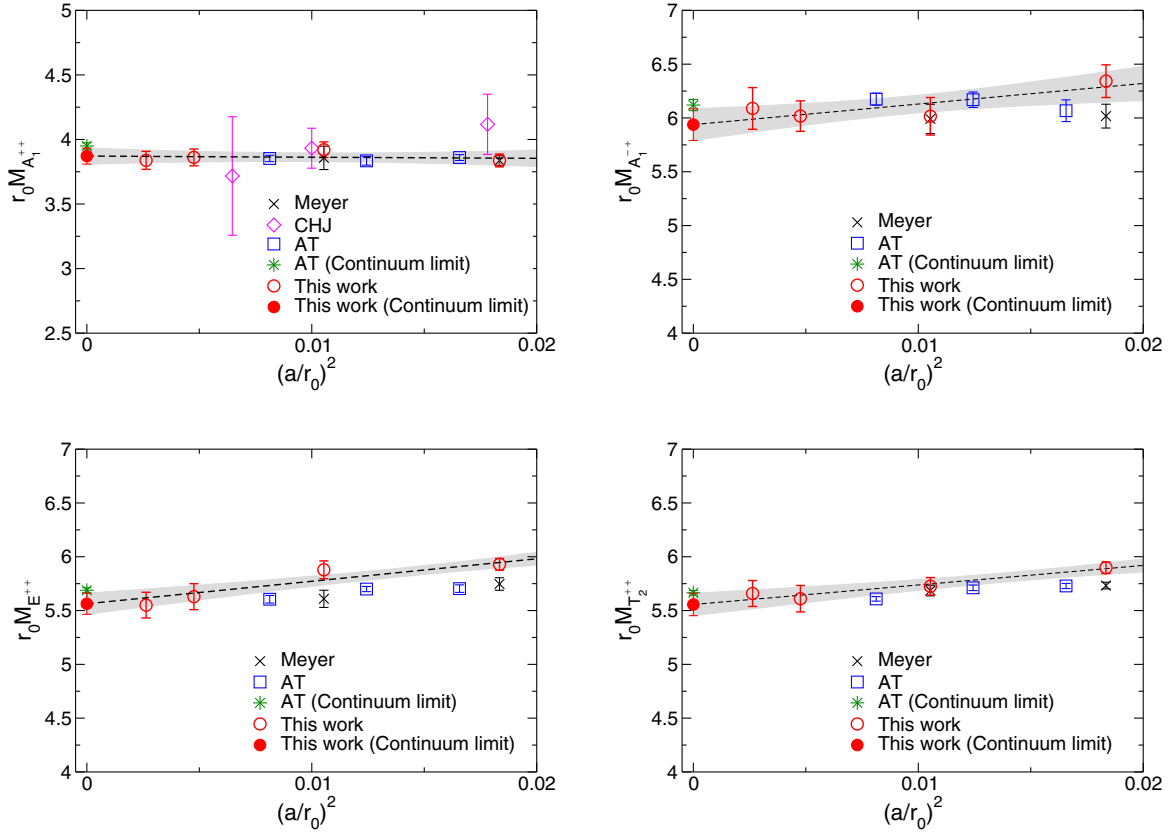

 FIG. 13. Comparisons of the glueball mass results for the ground states in the A_1^{++} (top-left), A_1^{-+} (top-right), E^{++} (bottom-left), and T_2^{++} (bottom-right) channels from this work, Meyer [7], CHJ [12], and AT [8]. Our results are calculated by the spatial gradient flow method. On the other hand, both the Meyer and AT results are given by the conventional approach, while the CHJ result are given by the ordinary gradient flow.

TABLE VIII. Comparison of the continuum-limit results of $r_0 M_G$ for the ground states of the A_1^{++} , E^{++} , T_2^{++} , and A_1^{+-} irreps. For comparison, the previous continuum-limit results are also included.

Irreps	This work	Meyer [7]	AT [8]	MP [5]	Chen [6]
A_1^{++}	3.871(62)(61)	3.883(79)	3.950(24)	4.21(11)	4.16(11)
E^{++}	5.563(98)(129)	5.703(106)	5.689(23)	5.85(2)	5.82(5)
T_2^{++}	5.556(104)(40)	5.658(75)	5.667(22)	5.85(2)	5.83(4)
A_1^{+-}	5.938(147)(132)	5.93(16)	6.120(52)	6.33(7)	6.25(6)

(top-right), E^{++} (bottom-left), and T_2^{++} (bottom-right) channels. Our results are calculated by the spatial gradient flow method. In each panel of Fig. 13, the dimensionless products of the glueball masses M_G and the Sommer scale r_0 are shown as functions of $(a/r_0)^2$ for a comparison with the previous works.

In the A_1^{++} channel, our results are fairly consistent with the previous works. On the other hand, although overall agreements with Meyer and AT results are observed in the other three channels, a more detailed comparison reveals a slight difference between these results and our results at the coarser lattice spacing. Especially, our data points calculated at $\beta = 6.2$ are slightly overestimated except for the A_1^{++} state. Nevertheless, our results obtained at the finer lattice spacings are consistent with the continuum-extrapolated AT result (marked as asterisk symbols) in all four channels.

We next perform the continuum extrapolation of the glueball masses $M_G(0)$ from the glueball masses $M_G(a)$ measured at the finite lattice spacing a . To remove the lattice discretization corrections on the measured glueball masses $M_G(a)$, we use a linear fit with respect to $(a/r_0)^2$ as

$$M_G(a)r_0 = c_0 + c_2 \left(\frac{a}{r_0}\right)^2 \quad (19)$$

with c_0 being the continuum-extrapolated glueball masses $M_G(0)$ in units of r_0 . The fit results using all four data points are shown in Fig. 13 as solid lines. The statistical uncertainty which is estimated by the jackknife analysis is indicated as the gray-shaded band in each panel. The data points are well described by the fitted curves. As mentioned above, our data points calculated at $\beta = 6.2$ are slightly overestimated in comparison to the previous works except for the A_1^{++} state, though our continuum results (marked as filled circles) are consistent with the continuum-extrapolated AT results obtained from their high-precision data in all four channels.

Our fit results are compiled in Table VIII. The quoted values of $r_0 M_G$ include a systematic error stemming from the continuum-extrapolation fits as the second error, which are evaluated from a difference between the fit results obtained by all four data points and three data points closest to the continuum. Table VIII also includes the previous continuum-limit results for comparison.

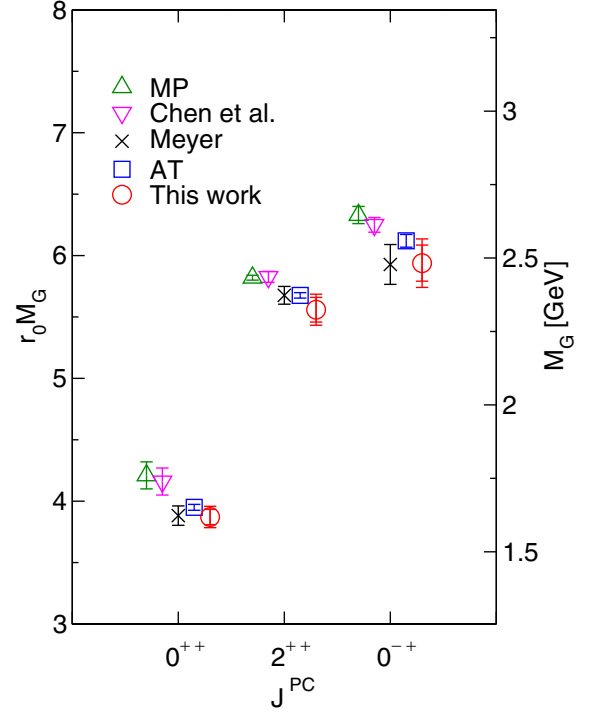


FIG. 14. Comparison of our continuum-limit results (circles) with the previous continuum-limit results: MP (upper triangles), Chen *et al.* (lower triangles), Meyer (cross symbols), and AT (squares) results, respectively. The masses are given in terms of the Sommer scale r_0 along the left vertical axis, while the right vertical axis is converted to physical units by $r_0 = 0.472$ fm, which is adopted in Ref. [8]. The inner and outer error bars on our results represent their statistical and total uncertainties, respectively.

In Fig. 14, we finally plot all of data included in Table VIII. The masses are given in terms of the Sommer scale r_0 along the left vertical axis, while the right vertical axis is converted to physical units by $r_0 = 0.472(5)$ fm,² which was adopted in Ref. [8]. For the 2^{++} results, we use a weighted average of $M_{2^{++}} = (2M_{E^{++}} + 3M_{T_2^{++}})/5$ for the final estimation. The inner and outer error bars on our results represent their statistical and total (adding statistical and systematic errors in quadrature)

²The quoted value is determined from $N_f > 2$ lattice QCD simulations in Ref. [27].

uncertainties, respectively. Our final results of the ground-states masses of the 0^{++} , 2^{++} , and 0^{-+} glueballs are obtained in physical units as follows:

$$M_{0^{++}} = 1.618(26)(25) \text{ GeV}, \quad (20)$$

$$M_{2^{++}} = 2.324(42)(32) \text{ GeV}, \quad (21)$$

$$M_{0^{-+}} = 2.483(61)(55) \text{ GeV}, \quad (22)$$

where the first error is statistical, while the second one represents a systematic error in the continuum extrapolation as explained above.

It is worth recalling that our results and the results of Meyer [7] and AT [8] are obtained from the isotropic lattice simulations, while the results given by Morningstar-Pearson [5] (denoted as MP result) and Chen *et al.* [6] are obtained from the anisotropic lattice simulations. The results from the isotropic lattice simulations are systematically underestimated in comparison to those of the anisotropic lattice simulations. This may suggest that there remains some subtlety in taking the continuum limit for the results obtained from the anisotropic lattice simulations. It is beyond the scope of this study, while our aim is rather to demonstrate the feasibility of our proposed approach. Furthermore, as discussed in Appendix B, we found that the spatial gradient flow is a few times more effective than the original gradient flow and the conventional approach. We therefore stress that the spatial gradient flow method can efficiently reproduce the recent high precision results of the glueball masses [8] within the statistical uncertainties.

VII. SUMMARY

We have studied the glueball two-point function with two types of the gradient flow method. The original gradient flow, which makes the Wilson flow diffused in the four-dimensional space-time, has some problem in measuring the glueball mass from the two-point function. It is known to be over smearing due to the overlap of two glueball operators extended in both space-time as reported in the previous study [12]. This particular issue makes the plateau behavior uncertain in the effective mass plot, so that it is difficult to extract the ground-state mass of the glueball with high accuracy.

To avoid over smearing, we propose the spatial gradient flow approach and also apply it to the glueball calculations. Our numerical simulations show that the spatial gradient flow method works well as a noise-reduction technique, meanwhile it has a good property that the plateau behavior in the effective mass plot does not change with variation in flow time for sufficiently large flow time. The latter point gives an advantage for extracting the ground-state mass of the glueball with high accuracy without over smearing.

It is also observed that the spatial gradient flow eliminates dependence of the Wilson loop shapes in the glueball two-point function due to a strong isotropic nature. Therefore, the variational method based on the different shapes is not applicable. Instead, the different diffuseness of the extended operator, which is given at the different flow time, are used for the variational analysis to separate the ground-state contribution from the excited-state contributions.

To demonstrate the feasibility of our proposed method, we have determined the masses of the three lowest-lying glueball states, corresponding to the 0^{++} , 2^{++} , and 0^{-+} glueballs, in the continuum limit by using four lattice QCD simulations for the lattice spacings ranging from 0.026 to 0.068 fm. Our results of the 0^{++} , 2^{++} , and 0^{-+} glueball masses are consistent with the previous works [7,8]. Especially, it is worth emphasizing that the spatial gradient flow method can efficiently reproduce the recent high-precision results [8], which are slightly underestimated in comparison to the results given by the anisotropic lattice simulations [5,6], within the statistical uncertainties.

We have also showed numerical equivalence between the spatial gradient flow and the stout smearing in the glueball calculations at the relatively fine lattice spacing of 0.0513(3) fm. This observation can be understood through the analytical derivation that demonstrates the equivalence between the gradient flow and stout smearing methods in the vicinity of the continuum limit as described in Appendix A. This fact can help to reflect actual efficiency for the glueball spectroscopy.

As discussed in Appendix B, although the spatial gradient flow requires several times fewer statistics to achieve the same statistical accuracy than the conventional method, its computational cost is roughly a factor of $\mathcal{O}(10)$ higher than the conventional one. Thus, by replacing the spatial gradient flow method with the stout smearing method, which is almost as computationally inexpensive as the conventional method, the gradient flow approach becomes really an efficient scheme for the glueball spectroscopy.

We plan to extend our research to calculate the glueball three-point function with the renormalized energy-momentum tensor formulated in the gradient flow method [28] in order to investigate the origin of the glueball masses. Such study is now in progress [29].

ACKNOWLEDGMENTS

K. S. is supported by Graduate Program on Physics for the Universe (GP-PU) of Tohoku University. Numerical calculations in this work were partially performed using Yukawa-21 at the Yukawa Institute Computer Facility, and also using Cygnus at Center for Computational Sciences (CCS), University of Tsukuba under Multidisciplinary

Cooperative Research Program of CCS (No. MCRP-2021-54 and No. MCRP-2022-42). This work was also supported in part by Grants-in-Aid for Scientific Research from the Ministry of Education, Culture, Sports, Science and Technology (No. 18K03605 and No. 22K03612).

APPENDIX A: EQUIVALENCE BETWEEN GRADIENT FLOW AND STOUT SMEARING

This section is devoted to a discussion of the equivalence between gradient flow and stout smearing referred in Sec. V B. For this purpose, we will first provide the explicit form of $\partial_{x,\mu} S_W[U]$ appeared in the left-hand side of Eq. (2).

The link derivative operator $\partial_{x,\mu}$ is defined as follows. The operator $\partial_{\mu,x}$ stands for the Lie algebra valued differential operator with respect to the link variable [9]. Let us introduce the anti-Hermitian traceless $N \times N$ matrices T^a ($a = 1, \dots, N^2 - 1$) as generators of $SU(N)$ group.³ In general, with respect to a basis T^a , the elements M of the Lie algebra of $SU(N)$ are given by $M = M^a T^a$ with real components M^a . Therefore, the operator $\partial_{x,\mu}$ can be expressed with respect to a basis T^a as

$$\partial_{\mu,x} = T^a \partial_{\mu,x}^a, \quad (\text{A1})$$

where the operators $\partial_{\mu,x}^a$ are defined by

$$\partial_{\mu,x}^a f(U) = \frac{d}{ds} f(e^{sX^a} U)|_{s=0} \quad (\text{A2})$$

with

$$X^a(y, \nu) = \begin{cases} T^a & \text{if } (y, \nu) = (x, \mu), \\ 0 & \text{otherwise,} \end{cases} \quad (\text{A3})$$

and act as differential operators on functions f of the link variable U .

When the link derivative $\partial_{x,\mu}$ acts on the action, we may simply focus on the term that explicitly depends on $U_\mu(x)$ in the action as

$$S_W[U] = -\frac{2}{g_0^2} \sum_{x,\mu>\nu} [\text{ReTr}\{U_\mu(x)X_\mu^\dagger(x)\} + \{\text{terms independent of } U_\mu(x)\}], \quad (\text{A4})$$

where $X_\mu(x)$ is the sum of all the path ordered products of the link variables, called the ‘‘staple’’. The staple $X_\mu(x)$ is given by

³In this paper, we use the notational conventions adopted in the original Lüscher’s paper [9]. Namely, they are normalized by $\text{Tr}(T^a T^b) = -\frac{1}{2} \delta^{ab}$ and also satisfy the commutation relations $[T^a, T^b] = f_{abc} T^c$ with the structure constants f^{abc} .

$$X_\mu(x) = \sum_{\mu>\nu} [U_\nu(x)U_\mu(x+\hat{\nu})U_\nu^\dagger(x+\hat{\mu}) + U_\nu^\dagger(x-\hat{\nu})U_\mu(x-\hat{\nu})U_\nu(x-\hat{\nu}+\hat{\mu})]. \quad (\text{A5})$$

If we set $\Omega_\mu(x) = X_\mu(x)U_\mu^\dagger(x)$, each basis component is given as

$$g_0^2 \partial_{\mu,x}^a S_W[U] = -2\text{ReTr}\{T^a \Omega_\mu^\dagger(x)\} = -\text{Tr}\{T^a (\Omega_\mu^\dagger(x) - \Omega_\mu(x))\}, \quad (\text{A6})$$

where $\Omega_\mu^\dagger(x)$ denotes the sum of all plaquettes that include $U_\mu(x)$. Therefore, we finally get

$$g_0^2 \partial_{\mu,x} S_W[U] = -iQ_\mu(x) \quad (\text{A7})$$

with

$$Q_\mu(x) = \frac{i}{2} (\Omega_\mu^\dagger(x) - \Omega_\mu(x)) - \frac{i}{2N} \text{Tr}(\Omega_\mu^\dagger(x) - \Omega_\mu(x)), \quad (\text{A8})$$

which becomes a Lie algebra valued quantity.

In the stout smearing, the link smearing is defined as the following recursive procedure [3]. Here, for simplicity, the stout smearing parameters $\rho_{\mu\nu}$ are taken as $\rho_{\mu\nu} = \rho$. The link variables $U_\mu^{(k)}(x)$ at step k are mapped into the link variables $U_\mu^{(k+1)}(x)$ using

$$U_\mu^{(k+1)}(x) = \exp(i\rho Q_\mu^{(k)}(x))U_\mu^{(k)}(x), \quad (\text{A9})$$

where $Q_\mu^{(k)}(x)$ is given by Eq. (A8) with the stout link $U_\mu^{(k)}(x)$ [3]. By taking the logarithm of both sides of Eq. (A9), one can get

$$\Delta_k \log U_\mu^{(k)}(x) = i\rho Q_\mu^{(k)}(x), \quad (\text{A10})$$

where Δ_k represents a forward difference with respect to k as $\Delta_k f(k) \equiv f(k+1) - f(k)$.

Next, let us introduce a continuous variable $s = k\rho$, and then reexpress the link variable $U_\mu^{(k)}(x)$ by writing a function of s as $\tilde{U}_\mu(x, s)$. Since $\frac{\partial}{\partial s} f(s) = \lim_{\rho \rightarrow 0} \frac{f(s+\rho) - f(s)}{\rho}$, the above difference equation (A10) becomes the differential equation with respect to the variable s in the limit of $\rho \rightarrow 0$.

$$\frac{\partial}{\partial s} \log \tilde{U}_\mu(x, s) = -g_0^2 \partial_{\mu,x} S_W[\tilde{U}], \quad (\text{A11})$$

TABLE IX. Comparison of effectiveness of respective smearing methods among three simulations (CHJ, AT, and this work) performed at the similar lattice spacing ($\beta \approx 6.4$). N_{total} denotes the number of total measurements in each simulation.

Label	β	$L^3 \times T$	N_{total}	Method	$aM_{A^{++}}$	EI
This work	6.40	$32^3 \times 32$	3000	Spatial gradient flow	0.404(9)	1.5
				Stout smearing (high n_{st})	0.403(9)	1.5
				Stout smearing (low n_{st})	0.442(31)	14.8
				Gradient flow ($R_d = 0.23$ fm)	0.446(14)	3.0
CHJ [12]	6.42	$32^3 \times 64$	1958	Gradient flow ($R_d = 0.3$ fm)	0.393(15)	2.9
				Gradient flow ($R_d = 0.35$ fm)	0.387(18)	4.3
AT [8]	6.338	$30^3 \times 30$	80000	Conventional approach	0.4276(37)	6.0

where the left-hand side of Eq. (A10) is rewritten by using the expression of Eq. (A7). Finally, Eq. (A11) reduces to a gradient flow equation with respect to the link variable $\tilde{U}_\mu(x, s)$ as

$$\frac{\partial}{\partial s} \tilde{U}_\mu(x, s) \cdot \{\tilde{U}_\mu(x, s)\}^{-1} = -g_0^2 \partial_{\mu,x} S_W[\tilde{U}] + \mathcal{O}(a) \quad (\text{A12})$$

in the vicinity of the continuum limit.⁴

It is clear that Eq. (A12) is equivalent to Eq. (2) at the leading order. Since the variable $s = k\rho$ directly corresponds to the Wilson flow time τ , the perturbative matching relation of τ , ρ and the number of stout smearing steps n_{st} as $\tau = \rho n_{\text{st}}$ found in Ref. [10] is also rigorously proved. Therefore, the gradient flow equation is certainly regarded as a continuous version of the recursive update procedure in the stout smearing at the smaller lattice spacing. When S_W is replaced by S_{sW} in the gradient flow equation, and $\rho_{\mu\nu}$ is set as $\rho_{ij} = \rho$ and $\rho_{4\mu} = \rho_{\mu 4} = 0$ in the stout smearing, above consideration fully supports our finding that there is the numerical equivalence between the spatial gradient flow and the spatial stout smearing in the glueball spectroscopy at the relatively fine lattice spacing of 0.0513(3) fm.

APPENDIX B: EFFECTIVENESS OF THE SPATIAL GRADIENT FLOW

In this appendix, we aim to assess effectiveness of our proposed method in comparison to the conventional

⁴When $U(s)$ is a matrix Lie group, $\frac{\partial U}{\partial s} U^{-1}$ is given in terms of $\frac{\partial}{\partial s} \log U$ as

$$\begin{aligned} \frac{\partial U}{\partial s} U^{-1} &= \frac{\partial}{\partial s} \log U + \frac{1}{2!} \left[\log U, \frac{\partial}{\partial s} \log U \right] \\ &+ \frac{1}{3!} \left[\log U, \left[\log U, \frac{\partial}{\partial s} \log U \right] \right] + \dots \end{aligned} \quad (\text{A13})$$

In the case when U is the link variable, the power series of $\log U$ in the left-hand side can be neglected for the small lattice spacing a .

approach. A simple indicator of effectiveness or efficiency of a given method to calculate the glueball mass is defined as the following index:

$$\text{Effectiveness index (EI)} = \left[\frac{(\text{Error})}{(\text{Central value})} \right]^2 \times (\text{No. of measurements}), \quad (\text{B1})$$

which is inversely proportional to the relative size of the square of the signal-to-noise ratio with respect to the statistics. When the EI index gets smaller, efficiency of the method becomes better with fixed statistics. Table IX compiles the values of effectiveness of respective smearing methods among three simulations (CHJ, AT, and this work) performed at the similar lattice spacing ($\beta \approx 6.4$). According to the EI value, the spatial gradient flow or the stout smearing with the high value of n_{st} is several times more effective than the original gradient flow and the conventional approach (see Ref. [30] for details of the smearing and fuzzing methods used in Ref. [8]).

It should be noted that the EI value does not reflect actual efficiency since the computational cost for the gradient flow method is relatively higher than the conventional approach. Indeed, in our actual numerical code, we find that the single-link smearing including APE smearing and stout smearing are a factor of $\mathcal{O}(10)$ faster than the gradient flow method even with the same numbers of flow iterations n_{flow} and smearing steps n_{st} . Moreover, the required number of flow iterations increases quadratically as the lattice spacing decreases.

Nevertheless, as numerically found in Sec. VB and analytically proven in Appendix B, the gradient flow method can be replaced by the stout smearing at the finer lattice spacing with keeping the same value of EI as shown in Table IX. Since the stout smearing is comparable to the conventional approach regarding the computational cost, the gradient flow approach is really an efficient scheme for the glueball spectroscopy and would have an advantage in dynamical lattice QCD simulations for glueball observables.

- [1] M. Albanese *et al.* (APE Collaboration), *Phys. Lett. B* **192**, 163 (1987).
- [2] A. Hasenfratz and F. Knechtli, *Phys. Rev. D* **64**, 034504 (2001).
- [3] C. Morningstar and M. J. Peardon, *Phys. Rev. D* **69**, 054501 (2004).
- [4] M. Teper, *Phys. Lett. B* **183**, 345 (1987).
- [5] C. J. Morningstar and M. J. Peardon, *Phys. Rev. D* **60**, 034509 (1999).
- [6] Y. Chen, A. Alexandru, S. J. Dong, T. Draper, I. Horvath, F. X. Lee, K. F. Liu, N. Mathur, C. Morningstar, M. Peardon *et al.*, *Phys. Rev. D* **73**, 014516 (2006).
- [7] H. B. Meyer, Glueball Regge trajectories, Ph.D. thesis, University of Oxford, [arXiv:hep-lat/0508002](https://arxiv.org/abs/hep-lat/0508002).
- [8] A. Athenodorou and M. Teper, *J. High Energy Phys.* **11** (2020) 172.
- [9] M. Lüscher, *J. High Energy Phys.* **08** (2010) 071; **03** (2014) 092(E).
- [10] C. Alexandrou, A. Athenodorou, K. Cichy, A. Dromard, E. Garcia-Ramos, K. Jansen, U. Wenger, and F. Zimmermann, *Eur. Phys. J. C* **80**, 424 (2020).
- [11] K. Sakai and S. Sasaki, *Proc. Sci. LATTICE2021* (2022) 333.
- [12] A. Chowdhury, A. Harindranath, and J. Maiti, *J. High Energy Phys.* **02** (2016) 134.
- [13] R. C. Johnson, *Phys. Lett.* **114B**, 147 (1982).
- [14] B. Berg and A. Billoire, *Nucl. Phys.* **B221**, 109 (1983).
- [15] C. Michael and M. Teper, *Nucl. Phys.* **B314**, 347 (1989).
- [16] C. Michael, *Nucl. Phys.* **B259**, 58 (1985).
- [17] M. Lüscher and U. Wolff, *Nucl. Phys.* **B339**, 222 (1990).
- [18] N. Cabibbo and E. Marinari, *Phys. Lett.* **119B**, 387 (1982).
- [19] M. Creutz, *Phys. Rev. D* **36**, 515 (1987).
- [20] R. Sommer, *Nucl. Phys.* **B411**, 839 (1994).
- [21] S. Necco and R. Sommer, *Nucl. Phys.* **B622**, 328 (2002).
- [22] N. Kamata and S. Sasaki, *Phys. Rev. D* **95**, 054501 (2017).
- [23] M. Lüscher and P. Weisz, *J. High Energy Phys.* **07** (2002) 049.
- [24] M. Lüscher, *Nucl. Phys.* **B180**, 317 (1981).
- [25] M. Teper, *Nucl. Phys.* **B411**, 855 (1994).
- [26] S. Sasaki and T. Yamazaki, *Phys. Rev. D* **74**, 114507 (2006).
- [27] R. Sommer, *Proc. Sci. LATTICE2013* (2014) 015 [arXiv:1401.3270].
- [28] H. Suzuki, *Prog. Theor. Exp. Phys.* **2013**, 083B03 (2013); **2015**, 079201(E) (2015).
- [29] K. Sakai and S. Sasaki (to be published).
- [30] B. Lucini, M. Teper, and U. Wenger, *J. High Energy Phys.* **06** (2004) 012.